

Metasurface-based total internal reflection microscopy

ANTU NEHUEN GORTARI,^{1,*} SOPHIE BOUCHOULE,¹ EDMOND CAMBRIL,¹ ANDREA CATTONI,¹ LARA HAUKE,² JÖRG ENDERLEIN,²  FLORIAN REHFELDT,² AND ALEJANDRO YACOMOTTI¹

¹*Ctr. de Nanosciences et de Nanotechnologies, Univ. Paris-Sud, Univ. Paris-Saclay, France*

²*Third Institute of Physics-Biophysics, Georg August University, Göttingen, Germany*

**antu-nehuen.gortari@c2n.upsaclay.fr*

Abstract: Recent years have seen a tremendous progress in the development of dielectric metasurfaces for visible light applications. Such metasurfaces are ultra-thin optical devices that can manipulate optical wavefronts in an arbitrary manner. Here, we present a newly developed metasurface which allows for coupling light into a microscopy coverslip to achieve total internal reflection (TIR) excitation. TIR fluorescence microscopy (TIRFM) is an important bioimaging technique used specifically to image cellular membranes or surface-localized molecules with high contrast and low background. Its most commonly used modality is objective-type TIRFM where one couples a focused excitation laser beam at the edge of the back focal aperture of an oil-immersion objective with high numerical aperture (N.A.) to realize a high incident-angle plane wave excitation above the critical TIR angle in sample space. However, this requires bulky and expensive objectives with a limited field-of-view (FOV). The metasurface which we describe here represents a low cost and easy-to-use alternative for TIRFM. It consists of periodic 2D arrays of asymmetric structures fabricated in TiO₂ on borosilicate glass. It couples up to 70% of the incident non-reflected light into the first diffraction order at an angle of 65° in glass, which is above the critical TIR angle for a glass-water interface. Only ~7% of the light leaks into propagating modes traversing the glass surface, thus minimizing any spurious background fluorescence originating far outside the glass substrate. We describe in detail design and fabrication of the metasurface, and validate its applicability for TIRFM by imaging immunostained human mesenchymal stem cells over a FOV of 200 μm x 200 μm. We envision that these kinds of metasurfaces can become a valuable tool for low-cost and TIRFM, offering high contrast, low photodamage, and high surface selectivity in fluorescence excitation and detection.

© 2020 Optical Society of America under the terms of the [OSA Open Access Publishing Agreement](#)

1. Introduction

During the last three decades, TIRFM has become an important microscopy technique for surface-restricted high-contrast and low-background fluorescence microscopy. [1–3] It is ideally suited to study cell membranes or surface-bound molecules. Most TIRFM applications use so-called objective-type TIR excitation (see e.g. [4,5]), where a focused laser beam is coupled into a high-N.A. objective at the edge of the back focal aperture to generate a plane-wave illumination in sample space, with an incidence angle above the critical TIR angle of the glass-sample interface. This then generates an evanescent excitation above the glass interface with a field intensity that exponentially decays with increasing distance from the interface. Such an approach requires oil-immersion objectives with a N.A. significantly larger than the refractive index of the cytoplasmic of a cell that can be as high as 1.4, i.e. an objective with N.A. >1.4. Besides being bulky and expensive, such objectives typically do not provide a large FOV.

In recent years, one has seen the rapid and broad development of a new generation of optical components, so-called optical metasurfaces (MSs), that can be seen as the two-dimensional variant of optical metamaterials and are expected to have a major impact on a wide range of next-generation of optical systems. MSs typically consist of periodic or quasi-periodic arrays of nanoresonators which modulate the phase of an incident wavefront in an arbitrary manner. This allows tailoring the phase properties of a wavefront in any desirable way, both in reflection and transmission mode. In contrast to traditional refractive optical elements, where phase changes of a propagating wavefront are accumulated rather gradually, a MS imparts an abrupt phase change on a propagating wavefront, usually on a length scale below one wavelength. This unique characteristic, along with the possibility to achieve arbitrary spatial phase modulation that is rather impossible to realize with conventional optical elements, has proven to be useful for a wide range of applications such as spectroscopy [6], integrated optics [7], optical filtering [8], multi-color imaging [9], holography [10,11], or biosensing [12].

State-of-the-art metasurfaces that are adapted to the visible spectrum can be especially important for optical microscopy, despite the relative scarcity of current efforts in this direction. Besides some impressive ongoing progress towards the development of achromatic metalenses (whose scope of applications goes well beyond microscopy), only few publications with relation to microscopy can be mentioned. Among them are the use of MSs to improve the axial resolution in laser scanning microscopy [13], the employment of metalenses for two-photon microscopy [14], the improvement of fluorescence-microscopy image contrast by using resonant structures [15], or the removal of orientation-induced localization errors in single-molecule localization microscopy [16,17].

Beam steering has been among the first pursued objectives in all MS developments, usually as first step towards more complex goals such as beam focusing. One of the first experimental realizations of this concept dates back by more than 20 years [18], with a binary grating more efficient than conventional “échelette” blazed gratings at high angles, where they are limited by their shadowing effect [19]. While the efficiency and complexity of these beam-steering MSs has increased significantly [20–23] with the advent of more advanced design tools (e.g. inverse design algorithms [21–23]) and nanofabrication technologies, to the best of our knowledge they were never used for MS-based TIRF microscopy.

The MS-based TIRF approach presented in this paper stems from a custom-designed MS and does not require any TIR-capable high-N.A. objective. Instead, a dedicated MS grating on the bottom of a glass coverslip redirects most of the incoming laser light (plane wave with perpendicular incidence angle with respect to the glass surface) into one of the first diffraction orders, thus acting as a blazed grating light-coupler. This generates a high-incidence angle wide field TIR illumination on the top side of the coverslip, with negligible propagation losses due to the extremely low extinction coefficient of the borosilicate glass in the visible range. We experimentally demonstrate that our MSs can couple up to 70% of the incident non-reflected light into the first diffraction order with a propagation angle of 65° with respect to the normal, which is sufficient for TIR excitation at the coverslip’s top surface. We demonstrate the applicability of these MS-substrates for TIRFM by imaging immunostained human mesenchymal stem cells (hMSCs) derived from whole bone marrow, which are often too large to be fully imaged by an objective-type TIRF system. In contrast to other recent experimental large-FOV TIRF techniques [24,25], this approach requires a single objective and the evanescent field’s penetration depth can be modified by adjusting the MS’s period or the angle of the incident beam.

This paper is organized as follows: in Section 2 we discuss the design, fabrication, and characterization of the TIRF-MS-Substrates. In Section 3, we apply them to fluorescence microscopy and bioimaging. Section 4 provides the final conclusions.

2. Metasurface design, fabrication, and characterization

When designing our MS we wanted to use only biocompatible materials that are transparent to light in the visible spectrum while maximizing the refractive index contrast between the MS nanostructure material and the substrate. Thus, we have chosen TiO_2 for the MS nanostructure material, and borosilicate glass for the substrate. The fabrication process of our MSs is as follows: A 230nm-thick layer of amorphous TiO_2 is deposited (Plassys MEB 800 IAD e-beam gun system) on a 25x50mm borosilicate glass. Two positive electron beam resists (A2 PMMA and EL10 MMA) are sequentially spin-coated to create a bilayer stack with a higher-sensitivity lower section, metalized with 20 nm of aluminum, and patterned using an electron beam writer (Raith EBPG-5000+). After a MIBK/IPA (1:3) resist development, the samples are rinsed in IP alcohol and a 20 nm nickel layer is deposited (Plassys MEB550SL e-beam evaporator). A lift-off process is performed in a trichloroethylene bath (85°C) followed by a HBr/BCl_3 TPSA-ICP TiO_2 reactive-ion etching. The remaining Ni is finally removed with a 1-min immersion in nitric acid 26%.

For the MS's design, we utilized the Rigorous Coupled-Wave Analysis (RCWA) software RETICOLO [26] to calculate the diffraction efficiencies and amplitudes of 2D stacked gratings. Starting from a 1D double groove structure (similar to those of [27] and [28]) and using a modified gradient ascent algorithm over hundreds of sets of 9 random initial dimensional parameters that define a generic structure layout, we converged to the design shown in Fig. 1(a) and (b). For this purpose, we defined and used a figure of merit (FOM) defined as the ratio between the diffraction efficiency of one of the first orders (-1) and the sum of the other two orders (i.e. 0^{th} and 1^{st}), resulting in an asymmetric composite layout of alternating continuous and segmented lines. This line segmentation was the optimal TiO_2 distribution when our current fabrication constraints were considered and allowed us to obtain the highest possible efficiency for a given maximum aspect ratio of the TiO_2 structures. The final sample is shown in Fig. 1(d).

The MSs were characterized by using an Olympus UApo N 100X 1.49 oil objective to collect all transmitted diffraction orders from the opposite side of the 170 μm glass substrate (the pair of first orders at a 65° angle would be internally reflected without the index-matching oil). The three transmitted beams are imaged by the objective into its back focal plane (BFP), which is then re-imaged on a CCD camera, thus allowing for the measurement of the three beam intensities and angles. The first order diffraction angle, being so relevant for our MS-TIRF device, was measured a second time with the help of a 100 mm semicylindrical prism oil-adhered to the MS coverslip, in which the beams can propagate long enough for a direct measurement using a photograph. Both measurements were in agreement with the theoretical value of 64.89°.

When the MS is illuminated at 90° incidence with TE-polarized light of $\lambda_0 = 640\text{nm}$ wavelength, we observe that 70% of the light entering the substrate is diffracted into the first diffraction order of interest (by design the one directed towards the center of the substrate), 21% is coupled in the opposite first order, and only 9% into the traversing zeroth order, as seen in Fig. 2. In terms of the total incidence intensity, these numbers are 43% and 13% for the first diffraction orders and 6% for the zeroth diffraction order, which means that 38% of the incident light is back-reflected. These values are in good agreement with the theoretically values of our RCWA calculations (55% and 16% for the first diffraction orders, 4% for the zeroth diffraction order, and 25% back-reflection). The small direct transmission of 4% is of key importance for the application of the MS to TIRFM, because it defines how much undesired fluorescence is excited deep in a sample far from the surface. The fact that most light sources in fluorescence microscopy are already polarized lasers greatly eliminates hurdles associated to using a TE-polarized only MS design.

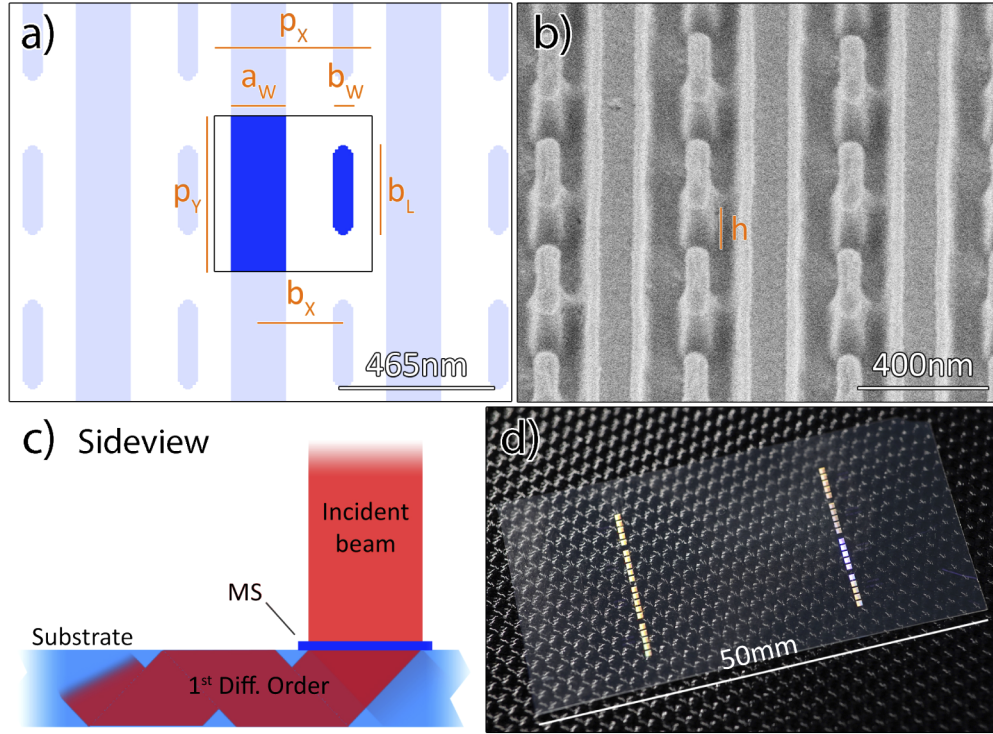


Fig. 1. (a) The horizontal geometry of the chosen 2D metasurface design for $\lambda_0 = 640\text{nm}$, with $p_x = p_y = 465\text{nm} = 0.73\lambda_0$, $a_w = 160\text{nm}$, $b_w = 61\text{nm}$, $b_x = 186\text{nm}$, $b_L = 322\text{nm}$, and a height $h = 230\text{nm}$ along with (b) a scanning electron microscope (SEM) image (45° tilt) of the fabricated sample. (c) When TE-polarized light hits the MS, up to 70% of the incident light is coupled into one of the first diffraction orders towards the center of the substrate, 21% is coupled into the opposite first order, and only 9% into the traversing zeroth order. (d) The entire $25 \times 50\text{ mm}$ substrate can accommodate multiple MSs, with 40 shown in this sample.

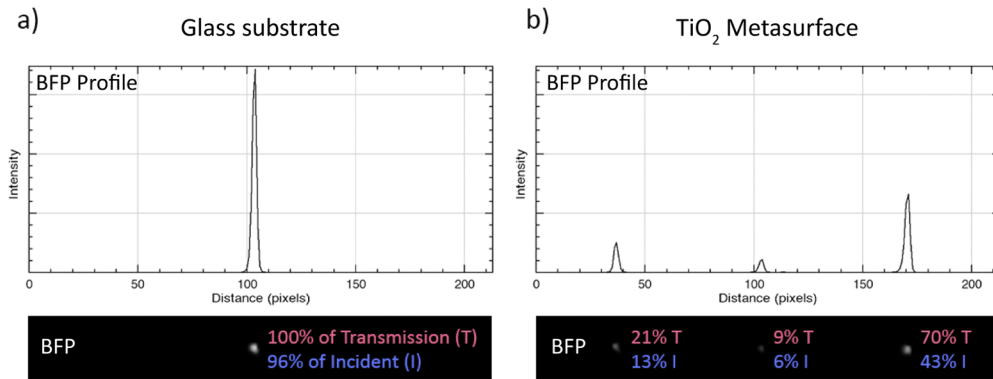


Fig. 2. When a TE incident beam hits the (a) plain glass substrate (reference) or (b) the MS, the images of the BFP allow for measuring the relative intensities of the different diffraction orders. Our MSs couples up to 70% of the light that enters the substrate into a diffraction order which propagates at a 65° angle with respect to the vertical, which being superior to the critical TIR angle, generates the desired evanescent field in sample space.

3. Fluorescence microscopy experimental setup and results

For MS-TIRFM we used the setup shown in Fig. 3. A motorized xy-stage with a dedicated metasurface holder is used for holding and moving the MS-substrate. Excitation and imaging is done with an Olympus UPlanSApo 40x NA 0.95 air objective mounted on both a motorized and a piezo z-stage (PIFOC, Physik Instrumente GmbH) allowing for fine and course vertical motion. Two continuous-wave diode lasers at 637 nm wavelength are used for simultaneous widefield (WF) and TIR illumination (Coherent OBIS 140 mW with a ZET 640/10 Laser Clean-up Filter). Imaging is done with an ANDOR iXon camera (Ultra DU-897U-CS0-#BV) which has a 512x512 pixel sensor (16 μm pixel size). The excitation light used for illuminating the MS was TE polarized using a Thorlabs CM1-PBS251 polarizing beam-splitter cube, and it was focused onto the MS by a Thorlabs AC254-300-A-ML 300 mm achromatic doublet.

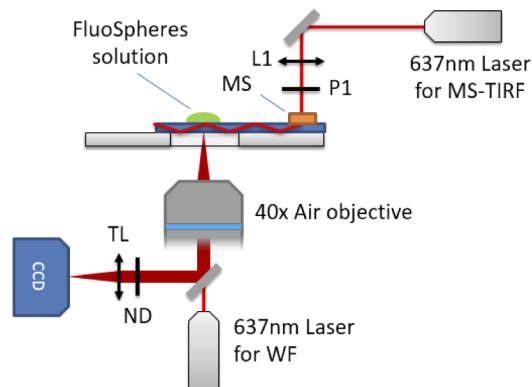


Fig. 3. The used microscopy setup allows to illuminate the sample both in TIR and WF illumination mode, using two 637 nm continuous-wave lasers. An Olympus UPlanSApo 40X NA 0.95 air objective and an ANDOR iXon Ultra camera are used to image the fluorescent sample which is mounted on a custom motorized stage. The lens L1 weakly focuses the incoming beam, which is linearly polarized by P1. The tube lens (TL) focuses the fluorescence light that is collected by the objective onto the CCD.

As a first test to verify we could selectively excite fluorophores in close proximity to the substrate's surface, while not exciting the bulk of a specimen, we placed and dried a highly diluted solution of fluorescent particles (Invitrogen FluoSpheres Carboxylate-Modified Microspheres, 0.2 μm , dark red fluorescent 660/680 0.0001% in volume) onto the substrate. This was followed by a second, larger (5-10 μl) droplet of solution, thus generating a sample with few particles attached to the surface and other particles diffusing freely in solution. After placing the sample on the microscope, we recorded continuous movies of fluorescence images while alternating between WF and MS-TIRF illumination, or both.

Figure 4(c) and (d) shows two frames of a series of 200 images, each with 100 ms integration time, resulting in a 20 seconds video. With 10 seconds of WF illumination, followed by 10 seconds of MS-TIRF illumination, we observe a clear difference between bright and dim particle images, corresponding to fluorescent beads attached to the surface, and to beads diffusing freely in solution but coming, for a short time, close to the surface into the evanescent field. With a frame time of 100 ms which is much longer than the average time needed by a diffusing particle to diffuse into and out of the evanescent field, no dynamics of this diffusion can be observed. However, when reducing the frame time, we more and more observe dynamic "blinking" events in a movie which capture a particle's diffusion into and out of the evanescent field in a time-dependent manner.

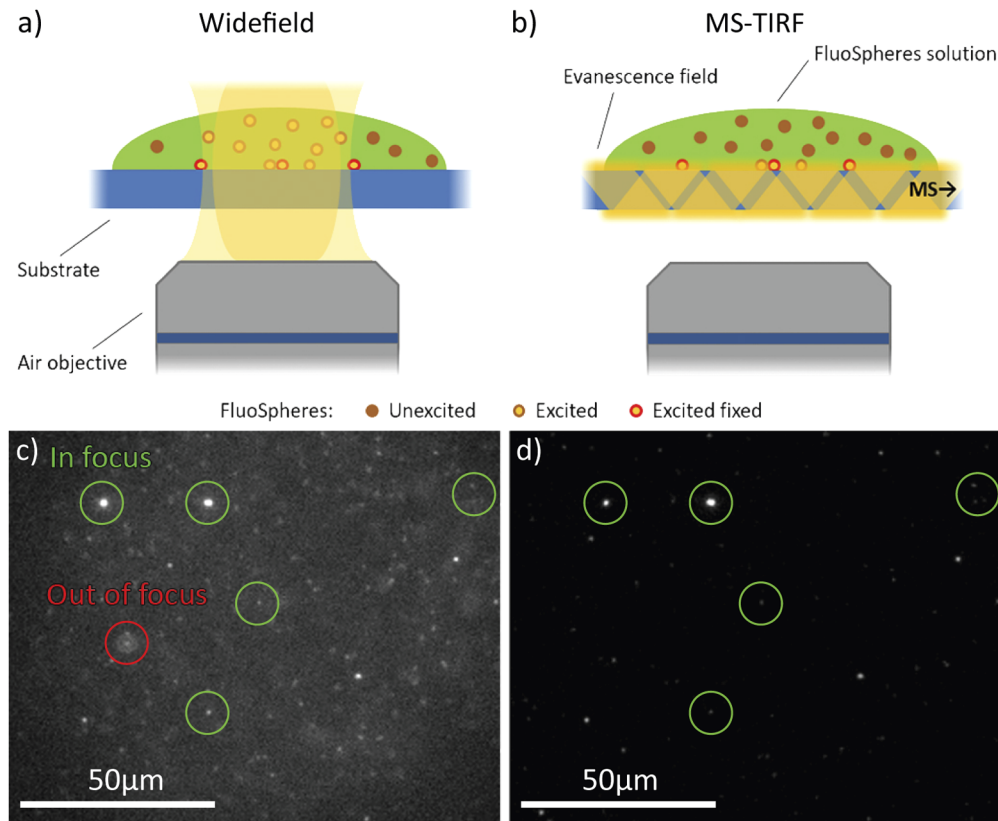


Fig. 4. The experimental setup visible in Fig. 3 was used to achieve widefield illumination (a), exciting all the fluorescent particles on the beam's vertical path, or TIRF illumination (b), exciting only those particles in close proximity to the substrate. Two frames of an image series of 0.2 μm Invitrogen FluoSpheres before (c) and after (d) switching from solely WF to solely MS-TIRF illumination. Integration time: 100 ms/frame. While WF illumination allows us to see the rapid motion of the diffusing particles in the bulk of the solution, it partially hides the fixed particles on the glass surface. MS-TIRF illumination selectively excites only those microspheres on the surface, eliminating the intense background generated by the diffusing particles in WF illumination (see [Visualization 1](#) for the full series). For shorter integration times, one observes occasionally particles diffusing from the bulk close to the surface generating short-time fluorescence intensity peaks when they pass through the evanescent excitation light.

Finally, by analyzing images recorded with MS-TIR excitation, see Fig. 4(d), we determined the maximum and mean brightness per pixel for the observed stationary fluorescent particles, and the standard deviation of the background (pixels not corresponding to particles). This allowed us to estimate a MS-TIRFM peak-signal-to-noise ratio (PSNR) superior to 700.

In order to exploit the exceptionally large FOV offered by MS-TIRF, we decided to image fixed hMSCs that were immunostained with anti-paxillin antibody (AB) and corresponding anti-rabbit IgG Atto 647N AB. Paxillin is an integral protein of the cell's focal adhesions, and it plays essential roles in important biological processes including motility, proliferation, differentiation, regulation of gene expression, and cell survival. The used primary antibody against paxillin does often also bind to targets in the cytosol making TIRF imaging particularly useful (see Fig. 5) for imaging paxillin in focal adhesions. In cell cultures, hMSCs can reach several hundred microns in diameter, often well beyond the FOV of conventional TIRF objectives. The detailed process for the sample preparation is found in the Appendix in Section 5.

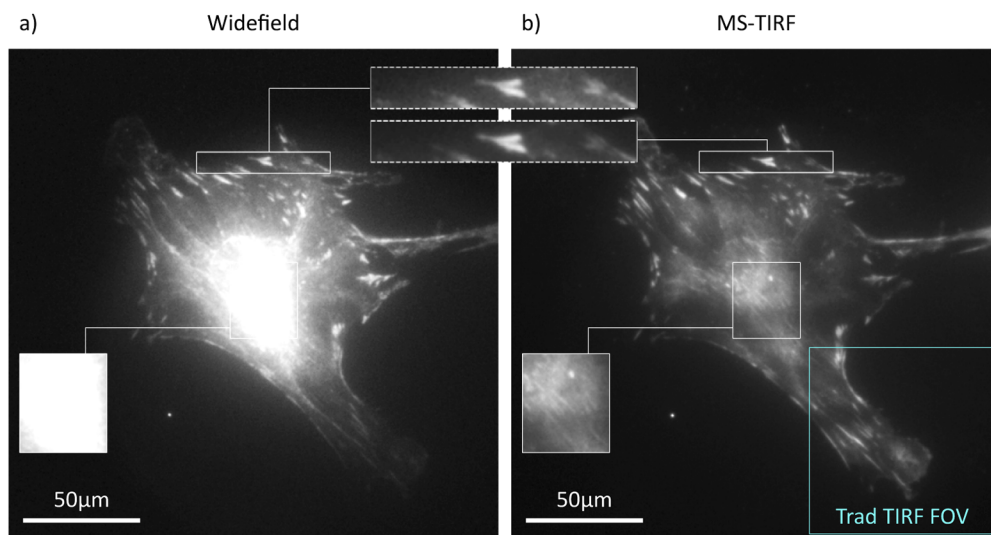


Fig. 5. Bone marrow hMSCs immunostained for focal adhesions with anti-paxillin AB and corresponding anti-rabbit IgG Atto 647N AB and imaged with (a) a standard WF microscope and (b) a MS-TIRF substrate. When equalizing the images' intensity with the brightness of the zones of interest (top dotted frames), background fluorescence originating from the cell's nucleus hides any information from the membrane below it (center (a) and (b)). For reference, the blue frame indicates the FOV of 80-100 μm obtainable with a typical 100x TIRF objective.

Using our MS-TIRF setup, we recorded a series of high-contrast images with the immunostained cells exclusively excited by the MS-generated evanescent field. Similarly to the FluoSpheres samples, one observes only a tiny slice of the cells close to the surface, thus greatly reducing background from the cells' interior. A representative image is shown in Fig. 5(b), where a clear distinction between the focal adhesions and the cell interior can be seen. Besides specific regions with high fluorophore concentration, Fig. 5(a) shows the existence of an even higher concentration in the endoplasmatic reticulum around the cell's nucleus, which is virtually invisible in the MS-TIRF image.

To better quantify the combined spatial resolution *and* FOV of our imaging modalities, we use the Space-Bandwidth Product (SBP), which can also be understood as the amount of information that an imaging system can transmit. The SBP can be expressed as the minimum amount of pixels on a sensor needed to capture all the information provided by the objective's resolution and

FOV. It can be easily calculated as the FOV surface divided by the pixel area required to achieve Nyquist sampling at the resolution given by the objective's N.A. and illumination wavelength. For the laser source and objectives as shown in Fig. 3, we calculated a SBP of 2.2 megapixels (100x, N.A. 1.49, FN=22, FOV=220 μm) and 8.2 megapixels (40x, N.A. 0.95, FN=26.5, FOV=660 μm). Thus, MS-based TIRFM delivers almost 4 times as much information than objective-type TIRFM. This number could climb up to almost 6 times by using a water 40x N.A. 1.2 water immersion objective, further reducing the resolution difference between the lower-N.A. objective used for MS-based TIRFM and the higher-N.A. oil immersion objective used for conventional objective-type TIRFM. Such an enlargement of the FOV and information bandwidth can be a valuable asset to automate imaging of slow-moving or large samples (e.g. the cells shown in this work), as well for biopsies of large specimens.

4. Conclusion

In this work, we introduced the concept of MS-TIRF microscopy. We designed, fabricated and experimentally tested various TiO_2 metasurface gratings capable of coupling as much as 70% of the incident non-reflected light into one of the two first diffraction orders, while greatly suppressing the direct transmission. Both are important conditions for a powerful TIRF coupling device. We used fluorescent micro-spheres to verify the selective illumination of MS-TIRF, and we measured the resulting signal-to-noise ratio. Moreover, we expect the efficiency of our MSs to increase significantly as recent improvements on the fabrication process allow for a 13% increase on the TiO_2 layer thickness, which translates in a full 2π phase coverage at $\lambda_0 = 640\text{nm}$. Finally, we imaged immunostained hMSCs using our MS-TIRF device and a 40x air objective, and we were able to obtain very high-contrast images over a FOV that was 9 times larger than that of traditional TIRF system. Furthermore, we calculated that the maximum SBP can be four times larger for the MS-TIRF system than for an objective-type TIRFM. While we have only used fixed cells in our study, no performance difference is to be expected for similar live samples.

In conclusion, we have shown that TiO_2 metasurface substrates provide a powerful alternative to high-N.A. objectives, enabling TIRFM with low-N.A. objectives. The wide flexibility of the MS design could also allow for implementing more advanced design features to tackle common weaknesses of multiple TIRFM techniques such as excitation inhomogeneity, that currently require expensive optomechanical systems (TIRF illuminators) to generate a spinning azimuthal incidence angle on the sample [29,30]. Future MSs could also allow for even higher axial selectivity by reducing the structure's period and thus increasing the TIR angle even beyond what is currently possible with TIRF objectives.

5. Appendix

The sample preparation consisted on the hMSC-bm cells (Lonza Ref. #PT-2501) grown in T75 cell culture flasks (Corning Inc., New York, NJ, USA, 43061) in Dulbecco's Modified Eagle Medium (DMEM Gibco, Thermo Fisher Scientific Inc., Waltham, MA, USA, A18967-01) supplemented with 10% fetal bovine serum (Sigma-Aldrich Co., St. Louis, MO, USA, F2442-500ML) and 1% antibiotics (penicillin/streptomycin, Life Technologies, Thermo Fisher Scientific Inc., Waltham, MA, USA, 15140-122) at 37°C and 5% CO_2 passaged every 2-3 days, with passage #5 was used for this experiment. Cells were seeded on non-coated 25 mm glass coverslips at a density of 10.000 hMSCs per glass in 6-well plates (Sarstedt AG & Co., Nuembrecht, Germany, 83.3920) with 2mL growth medium per well and grown at 37°C and 5% CO_2 . Cells were chemically fixed 24 h after seeding in a 10% formaldehyde (Sigma-Aldrich Co., St. Louis, MO, USA, 47608-250ML-F) in PBS for 10 min. Subsequently, cells were permeabilized using 0.5% Triton X 100 (Carl Roth GmbH & Co. KG, Karlsruhe, Germany, 6683.1) in PBS for 10 min and blocked with 3% BSA (Sigma-Aldrich Co., St. Louis, MO, USA, A9418-100G) in PBS for 30 min, incubated again with Triton X for 5 min and thoroughly washed with PBS. All antibodies

were kept in a 3% BSA PBS solution. Immunostaining was performed with anti-Paxillin (Abcam, ab32084) [1:400] for 10 h, then anti-rabbit IgG Atto 647N (Sigma-Aldrich Co., St. Louis, MO, USA, 40839) [1:400] for 2 h. Finally, the samples were covered with 24 mm glass coverslips using Fluoroshield mounting medium (Sigma- Aldrich Co., St. Louis, MO, USA, F6182-20ML).

Funding

H2020 Marie Skłodowska-Curie Actions (675512).

Acknowledgments

We thank Ingo Gregor, Soheil Mojiri and Oleksii Nevskyi (Third Institute of Physics - Biophysics, Georg August University, Göttingen, Germany) for their help with the TIRFM measurements.

Disclosures

The authors declare no conflicts of interest.

References

1. D. Axelrod, N. L. Thompson, and T. P. Burghardt, "Total internal reflection fluorescent microscopy," *J. Microsc.* **129**(1), 19–28 (1983).
2. D. Axelrod, T. P. Burghardt, and N. L. Thompson, "Total internal reflection fluorescence," *Annu. Rev. Biophys. Bioeng.* **13**(1), 247–268 (1984).
3. D. Axelrod, E. H. Hellen, and R. M. Fulbright, "Total internal reflection fluorescence," in *Topics in fluorescence spectroscopy*, (Springer, 2002), pp. 289–343.
4. M. Tokunaga, K. Kitamura, K. Saito, A. H. Iwane, and T. Yanagida, "Single molecule imaging of fluorophores and enzymatic reactions achieved by objective-type total internal reflection fluorescence microscopy," *Biochem. Biophys. Res. Commun.* **235**(1), 47–53 (1997).
5. M. Paige, E. Bjerneld, and W. Moerner, "A comparison of through-the-objective total internal reflection microscopy and epifluorescence microscopy for single-molecule fluorescence imaging," *Single Mol.* **2**(3), 191–201 (2001).
6. A. Pors, M. G. Nielsen, and S. I. Bozhevolnyi, "Plasmonic metagratings for simultaneous determination of stokes parameters," *Optica* **2**(8), 716–723 (2015).
7. D. Taillaert, F. Van Laere, M. Ayre, W. Bogaerts, D. Van Thourhout, P. Bienstman, and R. Baets, "Grating couplers for coupling between optical fibers and nanophotonic waveguides," *Jpn. J. Appl. Phys.* **45**(8A), 6071–6077 (2006).
8. C. J. Chang-Hasnain and W. Yang, "High-contrast gratings for integrated optoelectronics," *Adv. Opt. Photonics* **4**(3), 379–440 (2012).
9. B. H. Chen, P. C. Wu, V.-C. Su, Y.-C. Lai, C. H. Chu, I. C. Lee, J.-W. Chen, Y. H. Chen, Y.-C. Lan, C.-H. Kuan, and D. P. Tsai, "Gan metalens for pixel-level full-color routing at visible light," *Nano Lett.* **17**(10), 6345–6352 (2017).
10. P. Genevet and F. Capasso, "Holographic optical metasurfaces: a review of current progress," *Rep. Prog. Phys.* **78**(2), 024401 (2015).
11. H. Ren, G. Briere, X. Fang, P. Ni, R. Sawant, S. Héron, S. Chenot, S. Vézian, B. Damianno, V. Brändli, S. A. Maier, and P. Genevet, "Metasurface orbital angular momentum holography," *Nat. Commun.* **10**(1), 2986 (2019).
12. G. J. Triggs, Y. Wang, C. P. Reardon, M. Fischer, G. J. O. Evans, and T. F. Krauss, "Chirped guided-mode resonance biosensor," *Optica* **4**(2), 229–234 (2017).
13. D. Lee, M. Kim, J. Kim, H. Hong, T. Badloe, D. S. Kim, and J. Rho, "All-dielectric metasurface imaging platform applicable to laser scanning microscopy with enhanced axial resolution and wavelength selection," *Opt. Mater. Express* **9**(8), 3248–3259 (2019).
14. E. Arbabi, J. Li, R. J. Hutchins, S. M. Kamali, A. Arbabi, Y. Horie, P. Van Dorpe, V. Gradinaru, D. A. Wagenaar, and A. Faraon, "Two-photon microscopy with a double-wavelength metasurface objective lens," *Nano Lett.* **18**(8), 4943–4948 (2018).
15. M. Brunstein, A. Cattoni, L. Estrada, and A. M. Yacomotti, "Improving image contrast in fluorescence microscopy with nanostructured substrates," *Opt. Express* **23**(23), 29772–29778 (2015).
16. M. D. Lew and W. Moerner, "Azimuthal polarization filtering for accurate, precise, and robust single-molecule localization microscopy," *Nano Lett.* **14**(11), 6407–6413 (2014).
17. M. P. Backlund, A. Arbabi, P. N. Petrov, E. Arbabi, S. Saurabh, A. Faraon, and W. E. Moerner, "Removing orientation-induced localization biases in single-molecule microscopy using a broadband metasurface mask," *Nat. Photonics* **10**(7), 459–462 (2016).
18. P. Lalanne, S. Astilean, P. Chavel, E. Cambril, and H. Launois, "Blazed binary subwavelength gratings with efficiencies larger than those of conventional échelle gratings," *Opt. Lett.* **23**(14), 1081–1083 (1998).
19. P. Lalanne, S. Astilean, P. Chavel, E. Cambril, and H. Launois, "Design and fabrication of blazed binary diffractive elements with sampling periods smaller than the structural cutoff," *J. Opt. Soc. Am.* **16**(5), 1143–1156 (1999).

20. N. Yu, P. Genevet, M. A. Kats, F. Aieta, J.-P. Tetienne, F. Capasso, and Z. Gaburro, "Light propagation with phase discontinuities: Generalized laws of reflection and refraction," *Science* **334**(6054), 333–337 (2011).
21. D. Sell, J. Yang, S. Doshay, R. Yang, and J. A. Fan, "Large-angle, multifunctional metagratings based on freeform multimode geometries," *Nano Lett.* **17**(6), 3752–3757 (2017).
22. D. Sell, J. Yang, E. W. Wang, T. Phan, S. Doshay, and J. A. Fan, "Ultra-high-efficiency anomalous refraction with dielectric metasurfaces," *ACS Photonics* **5**(6), 2402–2407 (2018).
23. M. M. R. Elsayy, S. Lanteri, R. Duvinneau, M. S. Mohamed, G. Brière, and P. Genevet, "Global optimization of metasurface designs using statistical learning methods," (2019). Working paper or preprint.
24. S. Ramachandran, D. A. Cohen, A. P. Quist, and R. Lal, "High performance, led powered, waveguide based total internal reflection microscopy," *Sci. Rep.* **3**(1), 2133 (2013).
25. Ø. I. Helle, D. A. Coucheron, J.-C. Tinguely, C. I. Øie, and B. S. Ahluwalia, "Nanoscopy on-a-chip: super-resolution imaging on the millimeter scale," *Opt. Express* **27**(5), 6700–6710 (2019).
26. J. Hugonin and P. Lalanne, "Reticolo code 2d for analyzing 2d crossed grating," (2013).
27. T. Matsui, A. Miura, N. Ikeda, H. Fujikawa, Y. Sugimoto, N. Engheta, and H. Iizuka, "Experimental investigation of double-groove grating satisfying total internal reflection condition," *Opt. Express* **22**(21), 25362–25370 (2014).
28. D. Lin, M. Melli, E. Poliakov, P. S. Hilaire, S. Dhuey, C. Peroz, S. Cabrini, M. Brongersma, and M. Klug, "Optical metasurfaces for high angle steering at visible wavelengths," *Sci. Rep.* **7**, 2286 (2017).
29. A. L. Mattheyses, K. Shaw, and D. Axelrod, "Effective elimination of laser interference fringing in fluorescence microscopy by spinning azimuthal incidence angle," *Microsc. Res. Tech.* **69**(8), 642–647 (2006).
30. K. L. Ellefsen, J. L. Dynes, and I. Parker, "Spinning-spot shadowless tfr microscopy," *PLoS One* **10**(8), e0136055 (2015).